

A CMOS VEGF Sensor for Cancer Diagnosis Using a Peptide Aptamer-Based Functionalized Microneedle

Seungwoo Song, *Student Member, IEEE*, Jukwan Na, MoonHyung Jang, *Student Member, IEEE*, Hyeyeon Lee, *Student Member, IEEE*, Hye-Soo Lee, Yong-Beom Lim, Heonjin Choi, and Youngcheol Chae, *Senior Member, IEEE*

Abstract—This paper presents the first CMOS Vascular Endothelial Growth Factor (VEGF) sensor for cancer diagnosis directly from human blood. The sensor incorporates a peptide aptamer-based microneedle that allows the detection of electrochemical reactions with VEGF. This results in a capacitance change between the microneedles and then reads out by a two-step capacitance-to-digital converter (CDC). The proposed two-step CDC consists of a coarse 5b slope ADC and a fine 14b continuous-time delta-sigma modulator (CTDSM). During slow peptide-binding, the slope ADC performs a coarse conversion and the results are used to adjust the current level of the stimulator. After settling of the peptide-binding, based on an adjusted stimulation current, the CTDSM measures the small capacitance changes of the sensor. The prototype chip is fabricated in a 65-nm CMOS process, occupying a 0.87 mm² active area. The power consumption is 270 μ W. Thanks to the two-step approach, this work achieves a wide dynamic range of 18.3b, covering a large sensor-to-sensor variation. It also achieves a peak resolution of 13.7b, while maintaining <0.02% errors in 1 to 100 nF baseline capacitance. The overall sensor system successfully detects the VEGF in both phosphate-buffered saline (PBS) and human blood serum. Without the use of precision instruments, this work achieves a resolution of 15 fM_{rms} in range of 0.1 to 1000 pM and denotes the clear VEGF selectivity at 40x in PBS and 5x in the blood serum compared to other proteins (IgG, Con A, and cholera toxin).

Index Terms—Cancer biomarker, capacitance-to-digital converter (CDC), early cancer diagnosis (ECD), functionalized microneedle, negative-R assisted technique, peptide aptamer, vascular endothelial growth factor (VEGF), wide dynamic range (DR).

I. INTRODUCTION

ONE of the main causes of mortality to date is cancer. According to the World Health Organization (WHO), approximately more than 9.6 million people died of cancer only in 2018, and over 1 trillion US dollars were consumed for cancer treatment cost in 2010 [1]. Many early cancer diagnosis (ECD) techniques, which save lives and cut treatment costs

This work was supported by a National Research Foundation of Korea (NRF) grant funded by the Korea government (MSIP) (grant no. 2017R1A2B3011586), the Ministry of Science, ICT & Future Planning (2018M3C7A1024654). This work was supported by the IDEC, Korea. (*Corresponding author: Youngcheol Chae*)

S. Song, M. Jang, H. Lee and Y. Chae are with the Department of Electrical and Electronic Engineering, Yonsei University, Seoul, Republic of Korea (e-mail: ychae@yonsei.ac.kr)

J. Na, H.-S. Lee, Y.-B. Lim, and H. Choi are with the Department of Material Science and Engineering, Yonsei University, Seoul, Republic of Korea

effectively, already exist, such as imaging, endoscopy, and biopsy [2]. Imaging and endoscopy can detect tumors with a high detection rate; however, they cause discomfort such as radiation and pain with the requirement of bulky apparatuses. The biopsy is a cheap process and provides relatively less discomfort, but sample analysis takes a long time. In addition, these techniques can only be applied in hospitals and cannot be used for self-diagnosis. Moreover, more than half of the cancers are detected in less developed countries due to the lack of early detection and proper treatment [3]; thus, techniques different from the conventional ones are required for ECD in terms of time and cost.

A biomarker is a measurable indicator of a biological state, and the research on cancer biomarkers is actively underway [4]. Especially, vascular endothelial growth factor (VEGF), a signal protein produced by cells stimulating angiogenesis, is a key protein biomarker in cancer formation. A malignant tumor consists of rapidly dividing and growing cancer cells and requires a dedicated blood supply to provide oxygen and nutrients for growing a certain size. In this process, cancer cells secrete VEGF, and hence considered one of the key biomarkers for cancers [5]-[11]. Recently, biosensors have achieved considerable success in the detection and quantification of VEGF using synthetic receptors [7]. In particular, capacitive biosensors detect the change of dielectric properties when the receptor binds to VEGF, and the capacitance change can be used to quantify reactions. Since capacitive biosensors do not require large sample volumes, expensive antibodies, long incubation time, and complicated protocols, they are desirable for the early diagnosis of cancer. However, the sensitivity of capacitive biosensors still needs to be improved [7].

In this work, we present a capacitive biosensor for cancer diagnosis in human blood. The sensor involves aptamer-based functionalized microneedles with peptide receptors, and the electrochemical reaction with VEGF changes the capacitance between two microneedles. A large capacitance variation between the two microneedles is handled by an adaptive 5b current stimulator, and a small capacitance change due to the electrochemical reactions between the receptor and a small amount of VEGF can be readout by a high-resolution continuous-time delta-sigma modulator (CTDSM) and a low-pass filter (LPF). The proposed capacitance-to-digital converter (CDC) achieves a maximum resolution of 13.7b, and maintains under

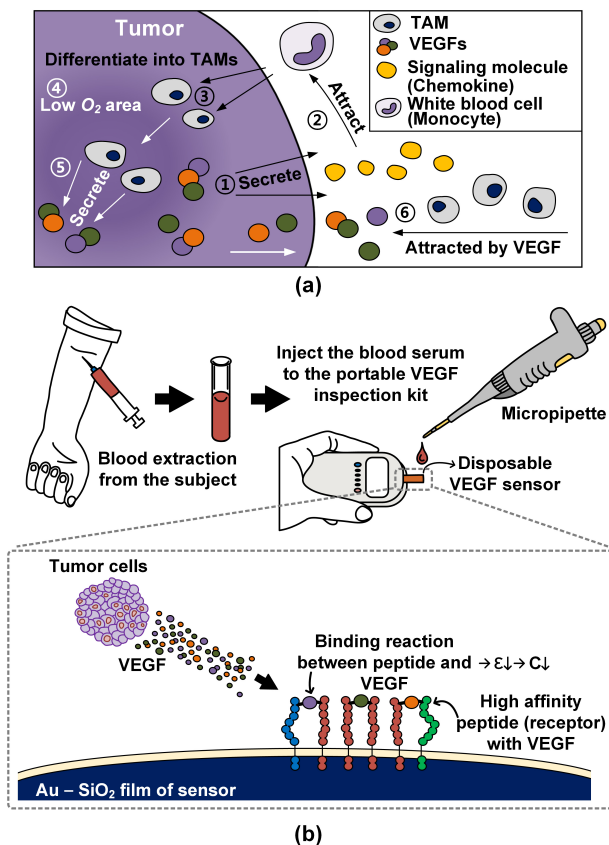


Fig. 1. (a) Positive feedback mechanism between VEGFs and TAMs, and (b) the peptide aptamer-based electrochemical sensing platform.

0.02% ($>12b$) resolution in 1 to 100 nF baseline capacitance (C_{base}). Fabricated in a 65-nm CMOS process with 270 μ W power consumption, it achieves competitive energy-efficiency Figure-of-Merit (FoM) in dynamic range (DR) (0.1 nJ/step) with 18.3b-DR while only occupying 0.87 mm² active area.

This work detects VEGF with a 15 fM_{rms} resolution over a wide detection range of 0.1 to 1000 pM, with 2x resolution improvement compared to prior works [8]-[11], and denotes the clear VEGF selectivity with 40x in phosphate-buffered saline (PBS) and 5x in blood serum compared to other proteins (IgG, Con A, and cholera toxin (CTx)) [12]. since this work is the first CMOS IC sensor system for cancer biomarkers using VEGF, the size of the sensor system is drastically reduced when compared to prior works.

This paper extends on an earlier report of the principle and demonstration in [12] and offers a detailed description of VEGF as cancer biomarker and peptide aptamer-sensor, fabrication of functionalized microneedle sensor, circuit implementation of the sensor readout IC, and a detailed analysis of the *in-vitro* measurement environment and results are described. This paper is organized as follows. Section II discusses a brief background of the VEGF detection principle and introduces a peptide aptamer-based biosensor. Section III describes the implementation of the functionalized microneedle. Section IV proposes a CMOS VEGF sensor system and Section V shows measurement results. Finally, conclusions are presented in Section VI.

II. BACKGROUND AND RELATED WORK

Aptamer-based biosensors, as VEGF detection methods for ECD, have drawn lots of attention due to their stability and target versatility [7]. In the aptamer-based biosensors, a wide variety of detection strategies exist for VEGF. In this paper, a peptide aptamer-based electrochemical sensing platform is chosen because the output electrical signal of this method is suitable for the electrical signal-based sensor readout.

A. Correlation between Various Cancers and VEGF

VEGF is considered as a cancer biomarker because of the positive feedback mechanism with tumor-associated macrophages (TAMs) [13]. TAMs are immune cells existing in large numbers in malignant tumors. Therefore, developing tumor cells generate numerous TAMs by the following series process shown in Fig. 1 (a). When the tumor develops, it secretes chemokines, a type of signaling molecules (①), and the chemokines attract circulating monocytes, known as white blood cells (②). Once the monocytes are dragged into the tumor, they are differentiated into TAMs (③). Then, TAMs in the tumor move to a low oxygen area (④) for secreting VEGFs to supply more oxygen (⑤). Finally, these secreted VEGFs re-attract TAMs (⑥). As a result, as the tumor develops, the amount of secreted VEGFs increases.

The correlation of various cancers with VEGFs has been also statistically demonstrated in [14]. The serum concentration of VEGF in the blood serum according to various cancers has been shown. In cancers of the digestive system, especially the gastric and colorectal cancer, higher the cancer stage be, the molar concentration of VEGF in the blood serum increases. However, when the unit is converted to molar concentration, the difference of VEGF in the blood serum is only few pM compared to that in a normal person and stage 1-3 cancer patients, which implies that a resolution for the detection of VEGF under the pM level is required.

B. Peptide Aptamer-Based Electrochemical Sensor

Aptamer-based biosensors are widely classified into two classes based on optical and electrochemical methods [7]. First, the optical aptamer-based biosensors are compact analytical devices with a biorecognition sensing element, but they require an optical transducer system for analyzing the optical signal output. On the other hand, electrochemical aptamer-based biosensors detect the electrical output signal, generated by the binding reaction between the synthetic molecules and biomarkers. In addition, various electrochemical techniques such as amperometric, potentiometric and impedimetric methods have been developed for more effective measurement. Therefore, the aptamer-based electrochemical sensing platform by using peptide receptors is chosen due to its suitable properties with respect to electric devices.

VEGF sensors for ECD have already been developed previously [7]. Among these sensors, the electrochemical aptamer-based VEGF sensors, whose type is the same as that of the proposed structure, are chosen for comparisons [8]-[11]. Similar to a previous work of ECD [8], the target specification

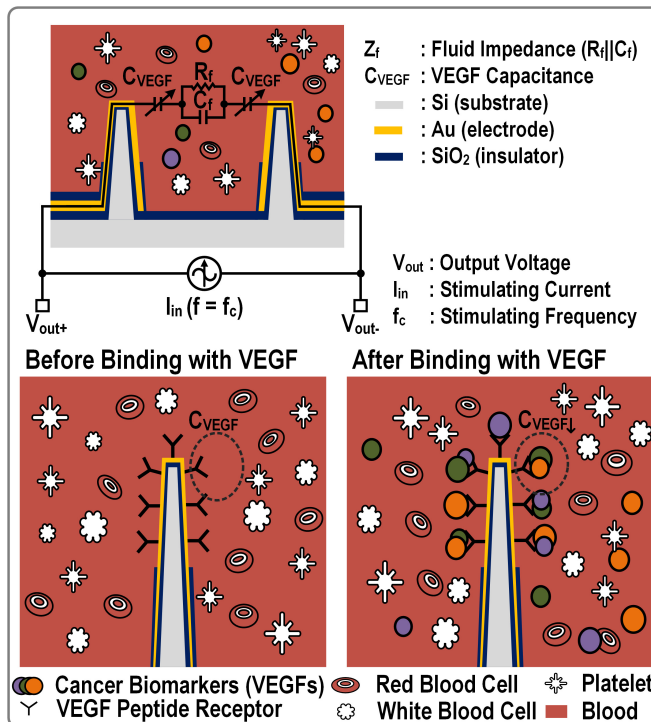


Fig. 2. Proposed VEGF sensor using a peptide aptamer-based functionalized microneedle.

of the sensor is determined as 0.1 pM of minimum VEGF detection limit, and <30 fM of VEGF resolution. However, since all these sensors only focus on the chemical-front-sensor, bulky measuring apparatuses are used such as potentiostat and galvanostat. Alternatively, a cost-effective measuring method is required such as impedance spectroscopy sensors implemented by CMOS [15]-[17].

III. FUNCTIONALIZED MICRONEEDLE

We developed a high-affinity self-assembled artificial peptide with VEGF, also called VEGF receptor, for the portable VEGF inspection sensor kit, and this was fabricated by acetylation process to the peptide V_{114} sequence, as specified in [5]. As shown in Fig. 1 (b), $AuSiO_2$ films of the sensor are coated with the high-affinity peptides with VEGF, and the binding reaction occurs when these peptides come into contact with VEGFs, secreted from tumor cells. This binding reaction changes permittivity (ϵ) between the $AuSiO_2$ films, resulting in capacitance variation. Specifically, the molar concentration of VEGF in the blood serum is inversely proportional to the capacitance between the peptide-coated $AuSiO_2$ films of the sensor.

Fig. 2 shows the electrochemical peptide aptamer-based functionalized microneedles. The silicon-based microneedle electrodes were fabricated by complementary metal-oxide-semiconductor technology as in our previous work [18]. A bare silicon (111) wafer was fabricated into micro-pillars by deep reactive-ion etching (DRIE), and sharpened into microneedles by wet etching process. Next, SiO_2 layer with the thickness of 300 nm was deposited as a primary insulating film by using

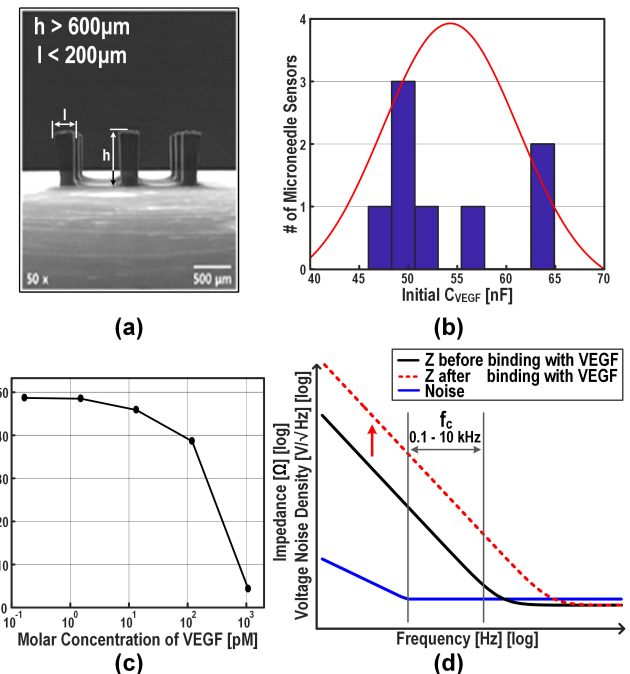


Fig. 3. Functionalized microneedle: (a) micrograph, (b) sensor-to-sensor capacitance variation, (c) capacitance variation with respect to VEGF concentration and (d) properties in frequency domain.

CMOS process, and Au electrode was formed on each microneedle. To minimize noise from outside, the secondary SiO_2 insulating film was deposited with the thickness of 300 nm except the microneedle area. Therefore, the microneedle has the structure of $Si-SiO_2-Au-SiO_2$ in cross-sectional view, and the end-tip of the microneedle has a pure Au layer without the secondary SiO_2 insulator. Additionally, the chemical reliability of the functionalized microneedles were verified with current stimulation of 50 μA .

This work aims to directly access the blood system or blood serum using the microneedle, and detects the targets in blood in real-time as shown in Fig. 2. The sensor is implemented with aptamer-based functionalized microneedles with peptide receptors, and the electrochemical reaction with VEGF changes the capacitance between the two microneedles.

Fig. 3 (a) shows the micrograph of the microneedles. The height of the microneedles is larger than $600\mu m$, and the length is less than $200\mu m$ to allow penetration below the dermis, but these properties result in relatively large sensor capacitance (C_{VEGF}) about 50 nF due to the large area (A) ($C = \epsilon \cdot (A/d)$, $d \approx 500\mu m$). The microneedle sensor is defined by a pair of microneedles, and C_{VEGF} is capacitance of the microneedle sensor. In addition, ϵ between the functionalized microneedles depends on the doping concentration of peptide and area of contact with the solution. Therefore, ϵ varies from case to case, resulting in the large sensor-to-sensor initial C_{VEGF} variation of 10 nF level, as shown in Fig. 3 (b). As shown in Fig. 3 (c), when a large amount of VEGF (about 1 nM) is injected, ΔC_{VEGF} varies more than 90% compared to the initial C_{VEGF} , C_{VEGF} becomes a few-nF. Fig. 3 (d) shows the sensor properties in the frequency domain. A noise

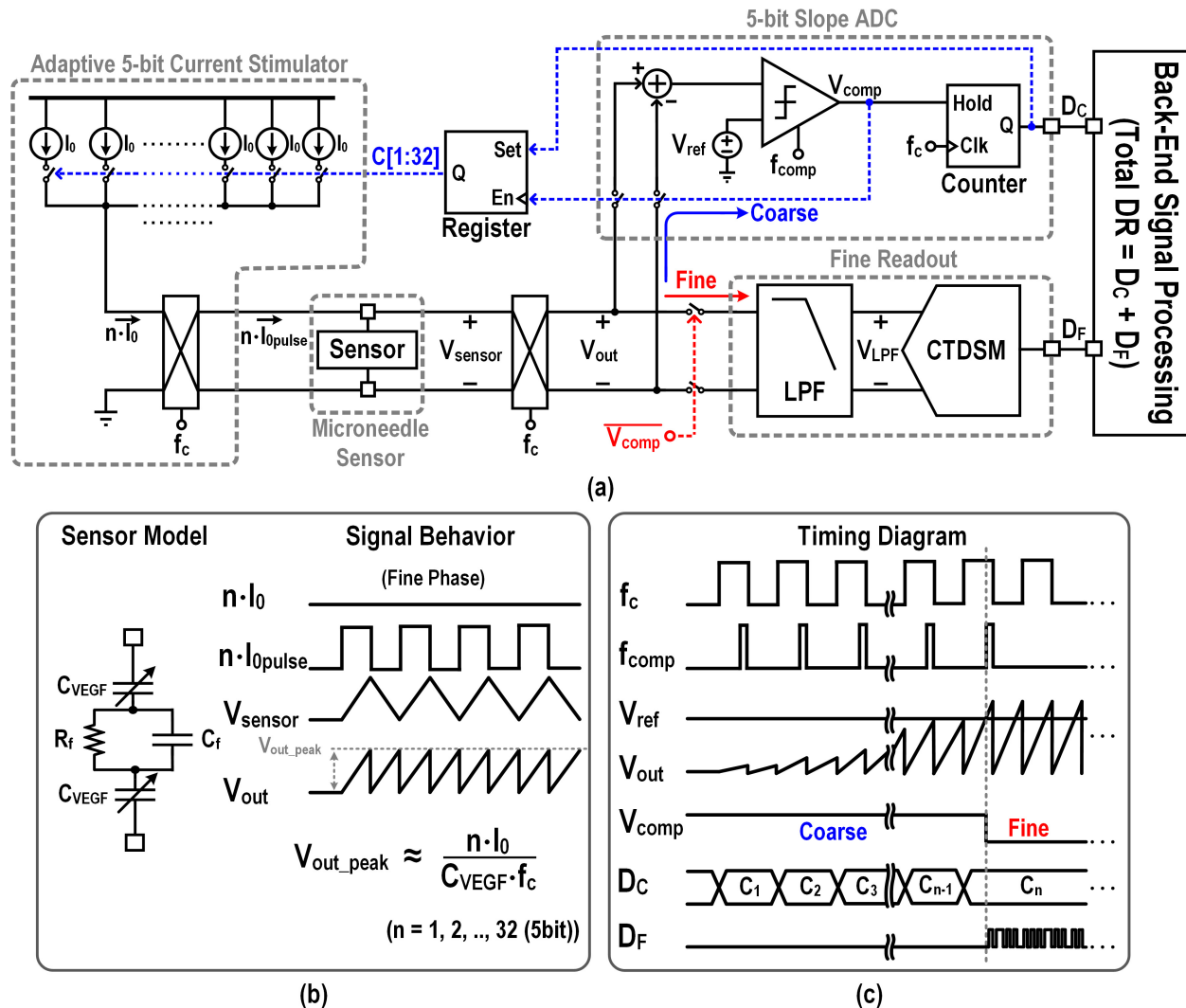


Fig. 4. (a) Full block diagram of the proposed sensor system, (b) sensor model and timing diagram in fine phase, (c) full timing diagram.

property of the electrode-based sensors commonly shows $1/f$ -like low-frequency drift noise behavior [19], [20], and the impedance should be measured in the low-noise frequency range for effective impedance analysis of electrode. Thus, the stimulation frequency f_c , which defines the frequency range of the impedance to be measured, should be carefully selected. Since the sensor's $1/f$ noise corner is about 0.1 kHz, so f_c is selected with a capacitively-operated and low noise frequency in the range of 0.1 to 10 kHz range.

IV. CMOS VEGF SENSOR

A. Design Requirements

As shown in Fig. 3 (b) and (c), the large sensor-to-sensor initial C_{VEGF} variation and large ΔC_{VEGF} are big challenges for the sensor readout. However, due to the simple structure of the prior CMOS impedance spectroscopy sensors [15]-[17], which was composed of the stimulator and readout frontend, it shows that the resolution and DR are proportional to power consumption. Especially, in wide DR application over 17b [17], large power over 20 mW is consumed. However,

in this case, the wide DR is required to cover the large sensor-to-sensor capacitance variation. Also, since this target application is a hand-held device for a real-time monitoring system, commonly operated by an internal battery, low power is required.

Since the functionalized microneedle sensor is a capacitance behavior-based sensor, a CDC structure could be implemented for the readout stage instead of the impedance sensor. Since the CDC only measures in-phase output, not including quadrature-phase output, the power consumption is reduced compared to the impedance sensor.

There are several key features of the proposed CDC. First, in case of direct VEGF measurement in the blood vessel, a regulated driving current ($<50 \mu\text{A}$) should be used to comply with the relevant medical standards [21] and also to guarantee the chemical reliability of the microneedles against the current. Second, an AC stimulator is implemented with f_c , and required wide DR due to the large capacitance variation is covered by implementing the adaptive current stimulator structure. Finally, high resolution under 30 fM target VEGF level, as

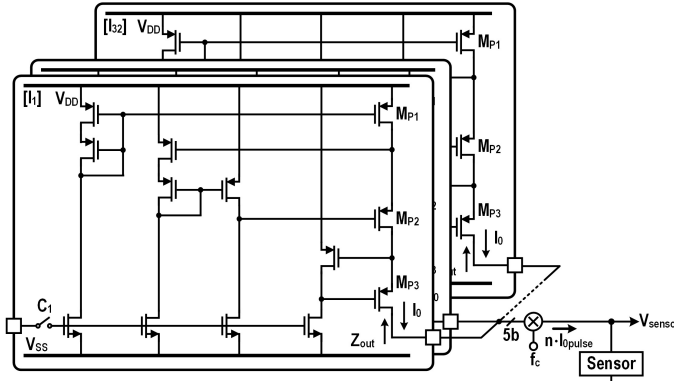


Fig. 5. 3-stack regulated cascode 5b-current stimulator.

in [8], is realized by a high-resolution LPF and CTDSM. In addition to the negative-R assisted CTDSM [22], the LPF is also configured by using the negative-R assisted technique.

B. Overall Architecture

The detailed full block diagram and timing diagram is shown in Fig. 4. As shown in Fig. 4 (a) and (b), the stimulator is implemented as the rectangular input current source ($n \cdot I_{0pulse}$), which is simply achieved by placing chopping switches with f_c after the input DC sources ($n \cdot I_0$). It injects $n \cdot I_{0pulse}$ to the microneedle sensor, and triangular voltage output (V_{sensor}) appears, due to the capacitance behavior-based sensor (C_{VEGF}). After then, the demodulation chopper, which located in front of LPF, converts V_{sensor} to V_{out} . Specifically, the peak output voltage ($V_{out,peak}$) could be approximated as

$$V_{out,peak} = \frac{n \cdot I_0}{(C_{VEGF} \oplus Z_f) \cdot f_c} \approx \frac{n \cdot I_0}{C_{VEGF} \cdot f_c} \quad (1)$$

when the fluid impedance ($Z_f = R_f \parallel C_f$) is negligible, where ($n = 1, 2, \dots, 32$ (5b)) and \oplus denotes series connection.

The full sensor system consists of two stages, the coarse and fine stage as shown in Fig. 4 (a). The coarse stage finds an appropriate input current level with 5b by using a coarse analog-to-digital converter (ADC), and fixes the current level of the stimulator when a proper sensor output voltage (V_{out}) is found through the adaptive 5b current stimulator. Then, V_{out} is accurately found through A/D conversion by the fine readout, which consists of LPF and CTDSM. Specifically, according to the full timing diagram in Fig. 4 (c), the adaptive 5b current stimulator is controlled by the 5b slope ADC (D_C), which compares V_{out} and the reference voltage (V_{ref}) with the comparison frequency (f_{comp}). The minimum current ($n = 1$) is injected, and until $V_{out} > V_{ref}$, the input current is increased ($n = 2, 3, \dots$). Finally, when $V_{out} > V_{ref}$, the input current, controlled by comparator output (V_{comp}), is fixed ($n = k$), and fixed V_{out} is transferred to the fine readout chain and starts fine A/D conversion (D_F). As a result, the resolution is determined by signal-to-noise ratio (SNR) of the fine readout, however, the total DR is expanded to the SNR of the fine readout (D_F) plus 5b of the coarse stage (D_C).

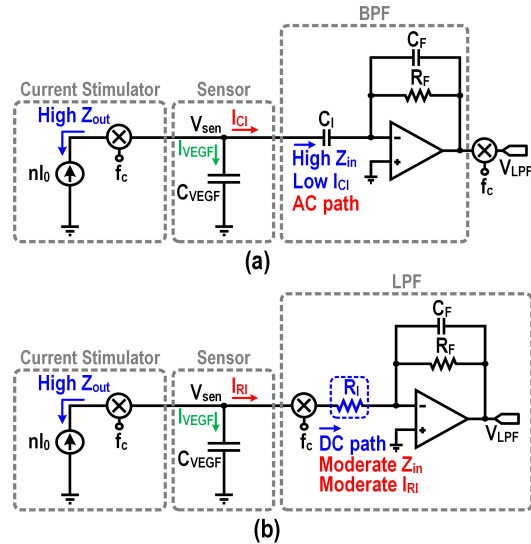


Fig. 6. Front-end with (a) capacitive input BPF and (b) resistive input LPF.

C. Stimulator

The adaptive 5b current stimulator is implemented with the current source array, and each current source is set to $1 \mu\text{A}$. Except for the low noise requirement, power-supply rejection ratio (PSRR) and output impedance (Z_{out}) of the stimulator are also critical issues for high performance. As shown in Fig. 5, each current source is implemented with a 3-stack regulated cascode structure with a 2.5-V supply. A large V_{GS} of M_{P1-3} makes M_{P1-3} get into a strong inversion region, which is advantageous to obtain a low output noise of the current source. However, the 3-stack cascode configuration makes V_{DS} of M_{P1-3} starve, resulting in large $\Delta I_D / \Delta V_{DS}$, thus poor PSRR. To enhance the PSRR, V_{GS} of M_{P1-3} is set to the moderate voltage $VDD/2$ with $VDD = 2.5$ V. From simulations, large PSRR of 72 dB is achieved with 10 mV, 1 kHz vibrating unstable power supply. In addition, the high Z_{out} over $200 \text{ M}\Omega$ of each current source is achieved by the 3-stack regulated cascode structure.

D. Readout with Negative-R Assisted LPF

The frequency components of triangular signal output (V_{out}) in Fig. 4 consist of a demodulated capacitance DC signal with lots of f_c harmonics. To mitigate these harmonics which cause signal aliasing, the fine readout stage is implemented with the LPF and CTDSM. The CTDSM is an appropriate choice because of its inherent anti-aliasing property. However, since the DC component of the V_{out} only accounts for half of the full signal, the signal loss occurs only when the DC component is accepted as a signal. Thus, to achieve high signal resolution, the noise of the readout should be as low as the small signal.

Fig. 6 shows the structure comparisons of each front-end. In the case of the capacitive input band-pass filter (BPF) [Fig. 6 (a)], due to the high Z_{out} of the current stimulator and C_{VEGF} , V_{sen} becomes a floating node. Thus, there is no DC path, and it could be hard to set the DC operating point of the sensor. Meanwhile, in the case of the resistive input LPF [Fig. 6 (b)]

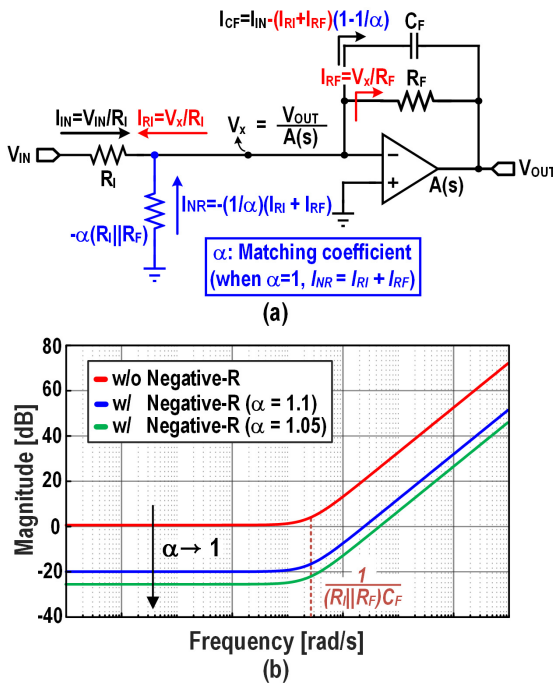


Fig. 7. (a) Principle of the active RC-LPF with negative-R assisted technique, and (b) transfer function of opamp noise.

which is chosen in this readout, input resistance R_I makes the DC path and sets DC operating point. However, R_I is in parallel with C_{VEGF} and makes lower $V_{out,peak}$ in Fig. 4 as

$$V_{out,peak} = \frac{n \cdot I_0}{(C_{VEGF} \parallel R_I) \cdot f_c}. \quad (2)$$

However, this is compensated by the 5b programmable current stimulator. Moreover, the negative-R assisted technique is configured which enhances the signal linearity and alleviates the noise of opamp in the LPF without increasing large power consumption.

Fig. 7 shows the principle of the negative-R assisted active RC-LPF. As shown in Fig. 7 (a), the finite gain of an opamp $A(s)$ makes a non-ideal virtual ground (V_X), and the input (R_I) and feedback resistance (R_F) are connected at V_X , which generates an error current ($I_{RI} + I_{RF}$). To compensate the error current, the negative-R is connected at V_X . The transconductance (g_m) value of negative-R is matched to $1/(R_I \parallel R_F)$, and α is the matching coefficient ($\alpha=1$ means ideal compensation). In details, the signal transfer function (STF) of V_{OUT}/V_{IN} could be denoted as

$$\frac{V_{OUT}}{V_{IN}} = -\frac{R_F}{R_I} \frac{1}{1 + R_F C_F s + \frac{1}{A(s)}(1 - \frac{1}{\alpha}) N L(s)} \quad (3)$$

where $N L(s) = 1 + R_F C_F s + R_F / R_I$, and this term is added by the error current, which aggravates noise and linearity of the RC-LPF. Meanwhile, when the negative-R is connected at V_X , the non-ideal portion in the STF is reduced with a ratio of α . In respect of the opamp noise transfer function (NTF) from the input of the opamp to the input of the LPF, it is given by

$$\frac{v_{n,in}^2}{v_{n,opamp}^2} = (1 + \frac{R_I}{R_F})^2 \{1 + s(R_I \parallel R_F) C_F\}^2 (1 - \frac{1}{\alpha})^2. \quad (4)$$

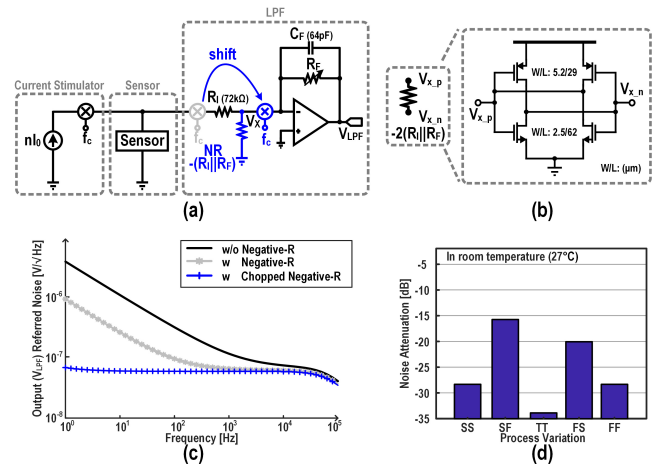


Fig. 8. (a) Simplified (single-ended) circuit diagram of the LPF, (b) schematic of the negative-R, (c) noise comparison of LPF, and (d) process variation vs. noise attenuation of the negative-R.

Therefore, without the negative-R, the opamp's noise is directly seen at the input node of the LPF. It results in stringent noise requirements of the opamp, which should be lower than the thermal noise level of the input and feedback resistors not to affect the overall noise. Whereas, with the negative-R, as the α gets closer to 1, the opamp noise is decreased as shown in Fig. 7 (b), so the opamp noise requirement is drastically reduced. However, the negative-R itself adds noise as $(R_I/R_N)^2 \cdot 4kT R_N$, where $R_N = -\alpha(R_I \parallel R_F)$. Therefore, the in-band input-referred noise of the negative-R assisted RC-LPF can be calculated as follows:

$$v_{n,in}^2 = 8kTR_I(1 + \frac{R_I}{R_F}) + |H(s)|^2 \cdot v_{n,opamp}^2 \quad (5)$$

where $|H(s)|^2$ is the opamp NTF with negative-R of (4). Since the opamp noise is attenuated by the negative-R, the noise requirement of the opamp can be considerably relaxed, resulting in a drastic power reduction of the opamp. In this LPF, 2x rms noise is reduced by increasing only 34 % power consumption when compared to the power of the opamp.

Fig. 8 shows the simplified circuit diagram of the LPF, schematic of negative-R, and noise property of LPF. In the LPF of Fig. 8 (a), R_I of 72 kΩ is selected to satisfy the target SNR (>12b) in several 100 mV levels of $V_{out,peak}$ with 1 to 100 nF C_{base} and 0.1 to 10 kHz f_c . Fig. 8 (b) shows the implementation of the negative-R with the differential-ended scheme. The negative-R is realized with two cross-coupled g_m stages. Even if the negative-R removes the noise of the opamp, the noise of the negative-R remains as shown in the grey line of Fig. 8 (c). By shifting the demodulation switches to the back of the negative-R, as shown in Fig. 8 (a), demodulation switches modulate 1/f noise of the negative-R as shown in the blue line of Fig. 8 (c).

In order not to affect the stability of the amplifier, the α of the negative-R is set over 1, which means that the error current is intentionally under-compensated not to saturate V_X by the negative-R. Also, the g_m variation of the negative-R due to the ΔV_X is <0.1%, because ΔV_X is only varied up to 300

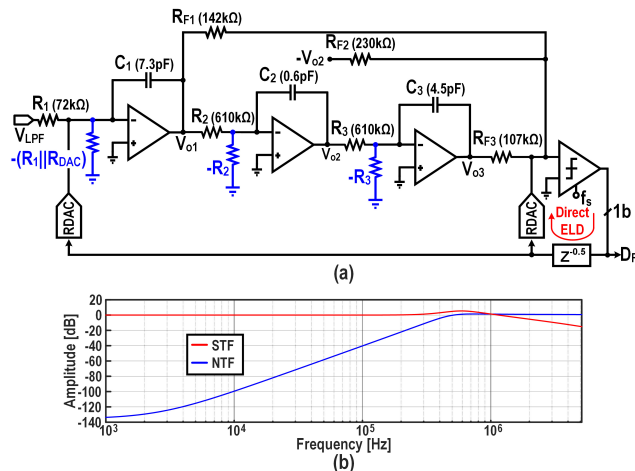


Fig. 9. (a) Simplified (single-ended) circuit diagram of the CTDSM, (b) STF and NTF of the CTDSM.

μV . As a result, the noise attenuation effect by the negative- R maintains <-16 dB according to the process variation as shown in Fig. 8 (d).

E. Negative- R Assisted CTDSM

The negative- R assisted technique is also implemented at the active RC-integrator, which is configured at the CTDSM as in [22]. Similar to RC-LPF in Fig. 7 (a), the error current (I_{RI} , $R_F = \infty$) is generated, and it is compensated by the negative- R . As a result, the STF of the RC-integrator could be denoted as

$$\frac{V_{OUT}}{V_{IN}} = -\frac{1}{R_I C_{FS} + \frac{1}{A(s)}(1 - \frac{1}{\alpha})(1 + R_I C_{FS})}. \quad (6)$$

The non-ideal portion in the STF of the RC-integrator is reduced with a ratio of α . In respect of the opamp NTF from the input of the opamp to the input of the LPF, it is given by

$$\frac{v_{n,in}^2}{v_{n,opamp}^2} = (1 - \frac{1}{\alpha} + R_I C_{FS})^2. \quad (7)$$

According to (7), as the α gets closer to 1, the opamp noise is decreased with high-pass filtering response.

Fig. 9 (a) shows a simplified schematic of the CTDSM, implemented using a 1b 3rd-order feed-forward structure with a resistive digital-to-analog converter (DAC) (RDAC). A direct path from V_{LPF} to the quantizer is omitted to improve anti-aliasing property. The loop filter consists of three negative- R assisted active-RC integrators to enhance in-band loop gain. Their DC-gain, gain-bandwidth (GBW), and slew-rate requirements are greatly relaxed by using the negative- R assistant [22]. A resistive adder is realized at the input of the quantizer, and compared to the single-bit CTDSM in [22], an excess-loop-delay (ELD) is improved by additionally implementing the direct feedback path to quantizer's input, resulting in lower operating frequency (f_s in Fig. 9 (a)) with 5.12 MHz, while maintaining BW (maximum usable BW is 20 kHz). As a result, it is denoted 95 (98) dB SNR in 20 (10) kHz BW with 68 μW power, resulting in 180 dB Schreier FoM with properly shaped STF and NTF as shown in Fig. 9 (b) (Schreier FoM = SNR+10log₁₀(BW/Power)).

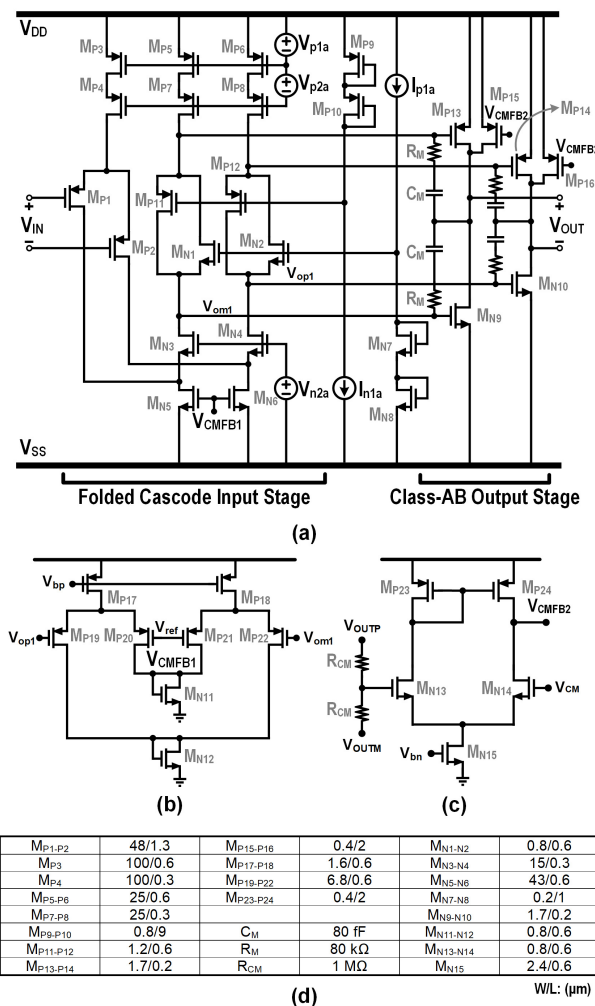


Fig. 10. Schematic of (a) opamp, (b) 1st stage CMFB, (c) output stage CMFB and (d) size of transistors.

F. Opamp Implementation

The folded cascode opamp with class-AB output stage, which consists of floating current source configuration and miller compensation structure as shown in Fig. 10 (a), is used in the LPF and 1st integrator of the CTDSM achieve g_m requirement with 72 $\text{k}\Omega$ input resistance, while consuming only 26 μA , thanks to the negative- R assisted topology. Originally, the required noise level of the opamp is determined by R_I (and R_F in case of the LPF), but negative- R relaxes the requirement. The class-AB output stage with floating current sources is designed to attain high output driving capability.

Common-mode feedback (CMFB) circuits of the opamp are shown in Fig. 10 (b) and (c). Each stage is assisted by CMFB circuits. Especially, CMFB in the output stage adopts resistive averaging method due to the large signal swing (1.1 $V_{peak-to-peak}$) [Fig. 10 (c)]. Meanwhile, since the 1st stage output voltage is not relatively large, CMFB of the 1st stage is configured by transistors to reduce the area [Fig. 10 (b)]. The transistors size specified in Fig. 10 (d) represent the values of the opamp in LPF and 1st integrator of CTDSM.

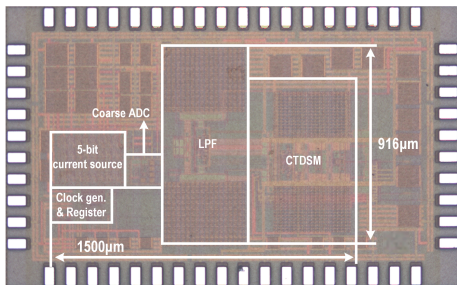


Fig. 11. Chip photograph.

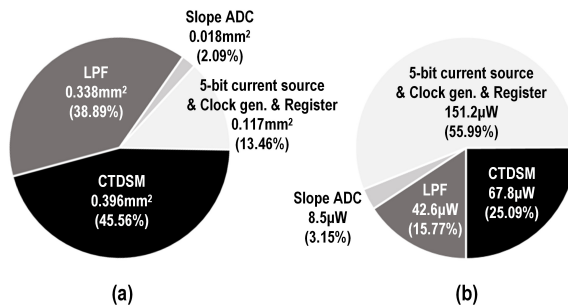


Fig. 12. (a) Area and (b) power breakdown of the proposed CDC.

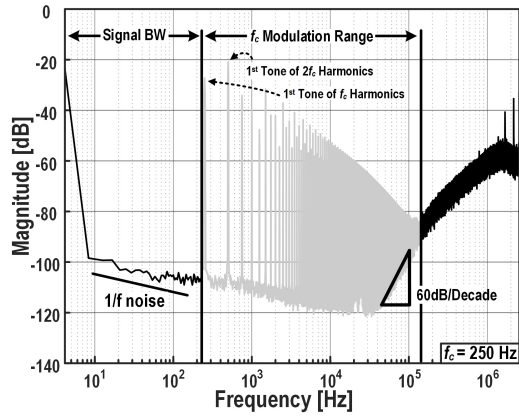


Fig. 13. Measured PSD of the proposed CDC with 250 Hz f_c .

V. MEASUREMENT RESULTS

The prototype CDC was fabricated in 65-nm standard CMOS process, only occupying an active area of 0.87 mm^2 as shown in Fig. 11. The supply voltage is 2.5-V for the coarse stage (5b current source, clock generator, register, and coarse ADC) and 1.2-V for the rest (fine readout). It consumes only $270 \mu\text{W}$, while the coarse stage dissipates $160 \mu\text{W}$. Fig. 12 shows the area and power breakdown diagram of the proposed CDC IC. CTDSM occupies half of the entire IC and most of the fine readout stage is filled with capacitors and resistors. The adaptive 5b current stimulator consumes more than half of the overall power because of the 2.5-V supply operation. The coarse 5b slope ADC uses only 2.1% of the total area and 3.2% of the overall power consumption.

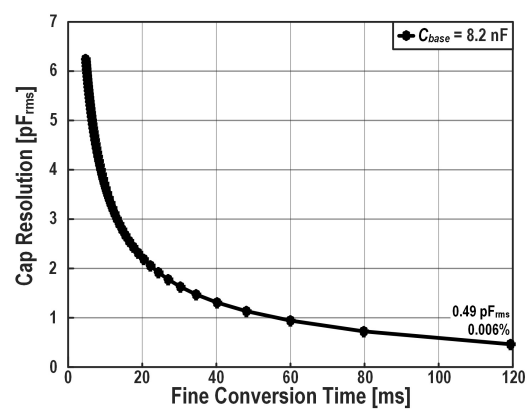


Fig. 14. Measured resolution vs. fine conversion time.

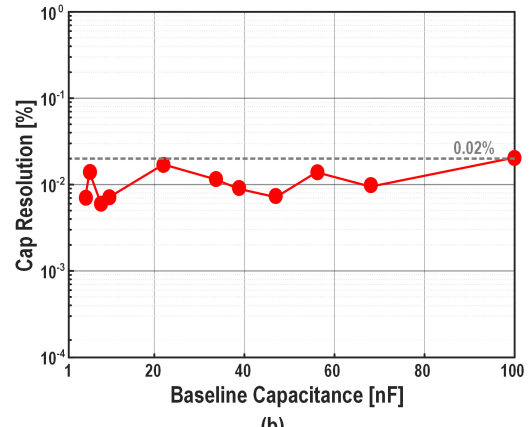
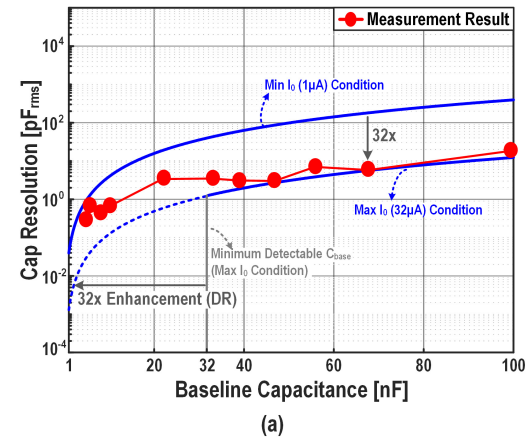


Fig. 15. Measured capacitance resolution under various baseline capacitances (a) [pF_{rms}], (b) [%].

A. Electrical Measurement Results

The performance of the proposed two-step CDC was verified by measuring the off-chip ceramic capacitors (1 to 100 nF). Fig. 13 shows the power spectral density (PSD) of the CDC for a sensor capacitor of 8.2 nF with $f_s = 5.12 \text{ MHz}$ of the CTDSM and $f_c = 250 \text{ Hz}$ of the stimulator. The signal BW is determined to $f_c (= 250 \text{ Hz})$, and the capacitance signal is located at DC. The filtered f_c harmonics by 1st-order RC-LPF are well located out-of-band, and the quantization-noise is 3rd-order properly shaped (60 dB/decade), regardless of f_c

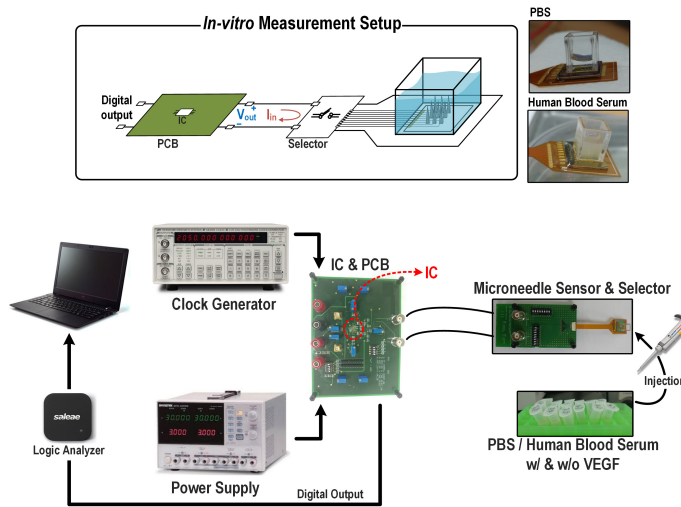


Fig. 16. *In-vitro* measurement setup.

harmonics. The $1/f$ noise comes from the limited matching property of the negative-R in the LPF. The DC component of the right-angled triangular signal, the output of the proposed CDC, is $1/2$ of the peak voltage. Nevertheless, thanks to its low noise level, the CDC achieves a maximum resolution of 13.7b. Fig. 14 shows the resolution of capacitance, as the conversion time increases. The $0.49 \text{ pF}_{\text{rms}}$ resolution is attained with 8.2 nF sensing capacitance in 120 ms conversion time, resulting in 13.7b maximum resolution.

Fig. 15 shows the measured capacitance resolution over the wide C_{base} range from 1 to 100 nF. As shown in Fig. 15 (a), the small capacitance in the maximum I_0 ($32 \mu\text{A}$) condition could not be measured due to the signal saturation, and the large capacitance in the minimum I_0 ($1 \mu\text{A}$) condition could not be measured due to small signal output. However, thanks to the proposed two-step structure, the total DR is $32\times$ enhanced than the SNR, and the capacitance resolution is maintained below 0.02% ($>12b$) in the 1 to 100 nF C_{base} range as shown in Fig. 15 (b).

B. In-vitro Measurement Results

The full sensor system including IC, receptor, and microneedles was validated through *in-vitro* measurement by using PBS and human blood serum. Fig. 16 shows the *in-vitro* measurement setup. The fabricated PCB connected IC, the power supply, and the clock generator, which provides f_c and f_s . The capacitance variation was measured by increasing VEGF concentration in the blood serum and PBS. Finally, the digital output was analyzed by a logic analyzer. Due to the yield issue of the functionalized microneedles, the measurement was proceeded using a paired with 9-microneedles sensor. During measurement, 2-microneedles were selected by a selector, and the other microneedles were maintained in floating state to keep high impedance not to affect C_{VEGF} . The electrochemical binding response between the peptides and VEGF takes time, up to 5 minutes. Therefore, every time VEGF was injected to the solution, it was necessary to wait for measuring the fixed signal after finishing the binding reaction.

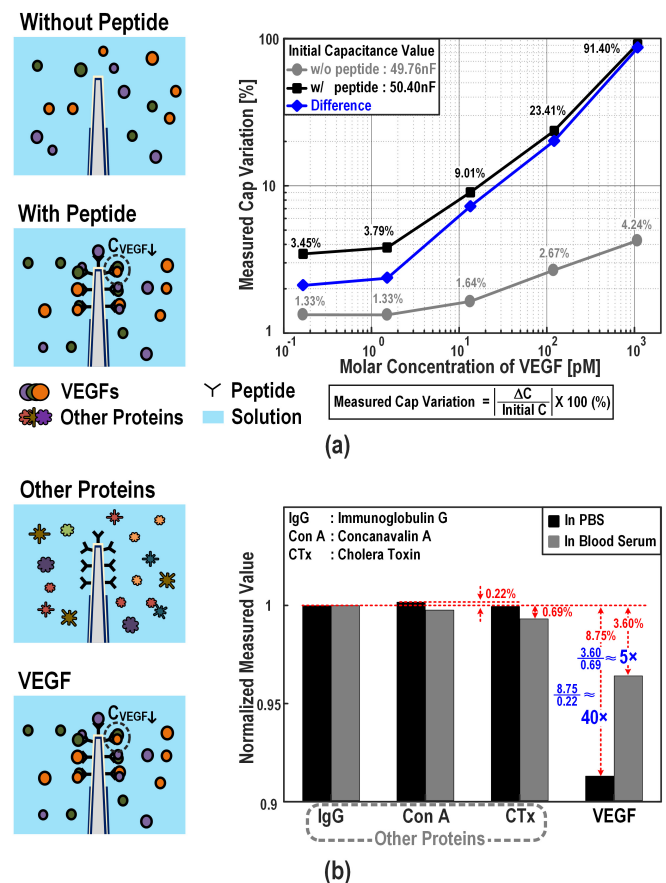


Fig. 17. *In-vitro* measurement results of the full sensor system: (a) Sensitivity: measured capacitance variation (%) with respect to VEGF concentration, and (b) Selectivity: comparison results with other proteins (IgG, Con A, and cholera toxin (CTx)) at the same concentration of injection (170 pM).

All experiments are conducted under an institutional review board (IRB) approval. We followed the standard protocol and all experimental solutions (the human blood serum, Con A, IgG, Cholera toxin, and VEGF (VEGF_{165}))) were supplied from Sigma-Aldrich.

The sensitivity test, as shown in Fig. 17 (a), was followed by increasing the VEGF gradually in the PBS. The microneedles without peptide do not bind with VEGF (grey circle line) and only capacitance variation occurs due to the change in molar concentration of a solution (varying 4.2% when injected with 1 nM VEGF). Since this capacitance variation is the error component, it should be removed by post-processing. Meanwhile, the peptide-coated functionalized microneedles (black square line) show a clear tendency to be proportional to the molar concentration of VEGF. After post-processing ((Normalized ΔC w/ peptide) – (Normalized ΔC w/o peptide)), the sensitivity denotes a $15 \text{ fM}_{\text{rms}}$ resolution in a range of 0.1 to 1000 pM (blue diamond line).

The selectivity of the sensor was also verified as shown in Fig. 17 (b). Since the VEGF sensor should only respond to VEGF, three other protein constructs, similar to VEGF, were used as the control group (IgG, Con A, and cholera toxin). Based on the pure PBS or blood serum as a solution, three other proteins were injected into the pure solution. After

TABLE I
PERFORMANCE SUMMARY AND COMPARISON WITH STATE-OF-THE-ART WORKS OF THE BIO-IMPEDANCE AND PHYSICAL SENSORS

Features		This work	JSSC'15 Helleputte [15]	VLSI'17 Ha [16]	ISSCC'18 Qu [17]
Application		Cancer Diagnosis	Bio-Impedance	Bio-Impedance	Gas Detection
Sensing Target		C	Z	Z	R
Architecture	Stimulator	Adaptive IDAC (Pulse)	IDAC (Pulse)	IDAC (Pulse)	VDAC (Sine)
	Readout	LPF + CTDSM	IA + PGA + LPF + DTDSM	IA + LPF + SAR	PGA + LPF + SAR
Technology [nm]		65	180	180	180
Area [mm ²]		0.87	-	2.52	15.12
¹ DR [bit]		18.3	12.5	11.0	17.1
² Resolution [bit]		13.7	12.5	11.0	17.1
Conversion Time [ms]		120	6.7	9	100
Power [μ W]	Stimulator	159.7	32.4	63.0	20600
	Readout	110.4	25.6	18.7	
Supply Voltage [V]		1.2/2.5	1.2	1.2/1.8	3
³ FoM _{DR} [nJ/Step]		0.1	*0.05	*0.22	14.66
⁴ FoM _{Resolution} [nJ/Step]		2.44	*0.05	*0.22	14.66

¹DR = $\log_2(\text{Maximum detectable } Z_{\text{base}}/\text{Minimum detectable } Z)$, ³FoM_{DR} = (Power×Conversion Time)/2^{DR}

²Resolution = $\log_2(Z_{\text{base}}/\text{Minimum detectable } Z)$, ⁴FoM_{Resolution} = (Power×Conversion Time)/2^{Resolution}

*In case of the impedance measurements, the power consumption of the single (for real) readout is included.

confirming that ΔC_{VEGF} hardly occurred, finally the VEGF was injected, resulting in large ΔC_{VEGF} . For comparison, the same quantity of proteins (170 pM) was injected, and each two-microneedle sensors were tested for each solution. As a result, it denotes the clear VEGF selectivity with 40× in PBS and 5× in blood serum compared to other proteins.

C. Comparison with Prior Works

Table I shows the summary of the state-of-the-art works on the impedance and physical sensors [15]-[17]. Due to the unique features of this work, it was hard to make a fair comparison with other biosensors. Because, most of them focus only on device-level chemical-front-sensors, i.e. without readout ICs. Since the system relies on the electrochemical impedance spectroscopy (EIS) principle for biomarkers, this paper was compared to the prior bio-impedance or physical sensor interfaces. For fair comparisons, in case of the impedance sensors in [15], [16], only the power consumption of the single readout was included when calculating FoM. Owing to the two-step CDC structure, this work achieves wider DR than that of other works, while not increasing large power consumption. Compared with bio-impedance interfaces, the high resolution with 13.7b, and the wide DR of 18.3b with a competitive energy-efficiency FoM-DR (0.1 nJ/step) are attained in this paper. Moreover, this work achieves even higher DR than that of recent work on the physical sensor

interface [17], but with significantly better energy-efficiency and 17× less area (0.87 mm²).

In addition, The biosensor detects VEGF with a 15 fM_{rms} resolution in the range of 0.1 to 1000 pM achieves 2× improvement compared to previous state-of-the-art work [8] and denotes clear selectivity of VEGF. Especially, compared to the prior VEGF sensors [8]-[11], which use high-end commercial products for VEGF measurement, measuring the VEGF using the sensor-specified CMOS IC allowed the size of the measuring system to be dramatically reduced.

VI. CONCLUSION

This paper proposes the first CMOS implemented capacitive biosensor IC to quantify the VEGF concentration in the blood to diagnose cancer at early stages. Specifically, the peptide aptamer-based functionalized microneedle allows electrochemical reactions with VEGF, resulting in a capacitance change between microneedles. The biosensor detects VEGF with a 15 fM_{rms} resolution in the range of 0.1 to 1000 pM and denotes clear selectivity of VEGF. Consequently, the peptide aptamer-based cancer biomarker detection system with the functionalized microneedle is a valuable technique for the first step of CMOS IC integrated biosensors intended for early cancer diagnosis.

REFERENCES

- [1] World Health Organization (WHO) [Online]. Available: <http://www.who.int/cancer/en/>
- [2] American Cancer Society [Online]. Available: <https://www.cancer.org/healthy/find-cancer-early/tests-to-find-and-diagnose-cancer.html>
- [3] B. W. Stewart, and C. P. Wild, *World Cancer Report 2014*, WHO.
- [4] G. C. Jayson *et al.*, "Plasma Tie2 is a tumor vascular response biomarker for VEGF inhibitors in metastatic colorectal cancer," *Nature Communications*, no. 4672, Nov. 2018.
- [5] W. J. Fairbrother *et al.*, "Novel peptides selected to bind vascular endothelial growth factor target the receptor-binding site," *Biochemistry*, 37, pp.17754–17764, Dec. 1998.
- [6] N. Ferrara, H-P. Gerber, and J. LeCouter, "The biology of VEGF and its receptors," *Nature Medicine*, vol. 9, no. 6, pp. 669-676, Jun. 2003.
- [7] S. Dehghani *et al.*, "Aptamer-based biosensors and nanosensors for the detection of vascular endothelial growth factor (VEGF): a review," *Biosensors and Bioelectronics*, vol. 110, pp. 23-37, Jul. 2018.
- [8] H. Da, H. Liu, Y. Zheng, R. Yuan, and Y. Chai, "A highly sensitive VEGF₁₆₅ photo-electrochemical biosensor fabricated by assembly of aptamer bridged DNA networks," *Biosensors and Bioelectronics*, vol. 101, pp. 213-218, Mar. 2018.
- [9] O. Kwon *et al.*, "Flexible FET-type VEGF aptasensor based on nitrogen-doped graphene converted from conducting polymer," *ACS Nano*, vol. 6, pp. 1486-1493, Jan. 2012.
- [10] S. Zhao, W. Yang, and R. Y. Lai, "A folding-based electrochemical aptasensor for detection of vascular endothelial growth factor in human whole blood," *Biosensors and Bioelectronics*, vol. 26, pp. 2442-2447, Jan. 2011.
- [11] M. A. Tabrizi, M. Shamsipur, R. Saber, and S. Sarkar, "Simultaneous determination of CYC and VEGF₁₆₅ tumor markers based on immobilization of flavin adenine dinucleotide and thionine as probes on reduced graphene oxide-poly(amidoamine)/gold nanocomposite modified dual working screen-printed electrode," *Sensors and Actuators B: Chemical*, vol. 240, pp. 1174-1181, Mar. 2017.
- [12] S. Song *et al.*, "A capacitive biosensor for cancer diagnosis using a functionalized microneedle and a 13.7b-resolution capacitance-to-digital converter from 1 to 100nF," *IEEE ISSCC Dig. Tech. Papers*, pp.194-195, Feb. 2019.
- [13] B. Samarasinghe, "The hallmarks of cancer 8: tumor-promoting inflammation," *Scientific American website*, Jan. 2015, [Online]. Available: <http://blogs.scientificamerican.com/guest-blog/2014/04/18/the-hallmarks-of-cancer-8-tumor-promoting-inflammation/>
- [14] I. Nakamura *et al.*, "Serum level of vascular endothelial growth factor are increased and correlate with malnutrition, immunosuppression involving MDSCs and systemic inflammation in patients with cancer of the digestive system," *Oncology Letters*, vol. 5, Issue. 5, pp. 1682-1686, Mar. 2013.
- [15] N. V. Helleputte *et al.*, "A 345 μ W multi-sensor biomedical SoC with bio-impedance, 3-channel ECG, motion artifact reduction, and integrated DSP," *IEEE J. Solid-State Circuits*, vol. 50, no. 1, pp. 230-244, Jan 2015.
- [16] H. Ha *et al.*, "A bio-impedance readout IC with frequency sweeping from 1k-to-1MHz for electrical impedance tomography," *IEEE Symp. VLSI Circuits*, pp.C174–C175, June 2017.
- [17] G. Qu *et al.*, "A 0.28m Ω -sensitivity 105dB-dynamic-range electrochemical impedance spectroscopy SoC for electrochemical gas detection," *IEEE ISSCC Dig. Tech. Papers*, pp.286-287, Feb. 2018.
- [18] J. Na *et al.*, "Real-time detection of markers in blood," *Nano Letters*, 19 (4), pp. 2291-2298, Mar. 2019.
- [19] Y. M. Chi, T-P. Jung, and G. Cauwenberghs, "Dry-contact and noncontact biopotential electrodes: methodological review," *IEEE Review In Biomedical Engineering*, vol. 3, pp. 106-119, Oct. 2010.
- [20] S. Ha *et al.*, "Integrated circuits and electrode interfaces for noninvasive physiological monitoring," *IEEE Trans. On Biomedical Engineering*, vol. 61, No. 5, pp. 1522-1537, May. 2014.
- [21] Medical Electrical Equipment. Part 1: General Requirements for Safety and Essential Performance, IEC 60601-1, 2000.
- [22] M. Jang, C. Lee, and Y. Chae, "Analysis and design of low-power continuous-time delta-sigma modulator using negative-R assisted integrator," *IEEE J. Solid-State Circuits*, vol. 54, no. 1, pp. 277-287, Jan 2019.



Seungwoo Song (S'13) received the B.S. degree in electrical and electronic engineering from Yonsei University, Seoul, Korea, in 2013. He is currently working toward a Ph.D. degree in electrical and electronic engineering at Yonsei University, Seoul, Korea.

His current research interests include precision amplifier, biosensor, delta-sigma modulator, and low noise sensor interfaces.



Jukwan Na (S'14) received a B.S degree in materials science and engineering from the University of Seoul, Seoul, Korea in 2014. He is currently working toward a Ph.D. degree in materials science and engineering from Yonsei University, Seoul, Korea.

His current research interests include 3D type of biosensors, growth of 1D nanomaterials, and fabrication of device via CMOS process.



MoonHyung Jang (S'16) received the B.S. degree (*summa cum laude*) in electrical and electronic engineering from Yonsei University, Seoul, Korea, in 2014. He is currently working toward a Ph.D. degree in electrical and electronic engineering at Yonsei University, Seoul, Korea.

His current research interests include continuous-time delta-sigma modulator, hybrid ADCs, high precision analog circuits, and low noise sensor interfaces.

Mr. Jang received a bronze prize in the Samsung HumanTech Paper Award in 2018.



Hyeyeon Lee (S'16) received the B.S. degree in electrical and electronic engineering from Yonsei University, Seoul, Korea, in 2016. She is currently working toward a Ph.D. degree in electrical and electronic engineering at Yonsei University, Seoul, Korea.

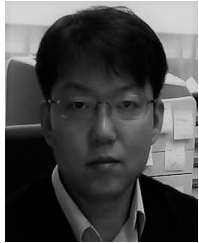
Her current research interests include capacitive sensor interfaces.

She received a National Scholarship for Science and Engineering from KOSAF, (Korea Student Aid Foundation), from 2014-2015. She is being supported by the NRF (National Research Foundation of Korea) Grant funded by the Korean Government (NRF-2017-Fostering Core Leaders of the Future Basic Science Program/Global Ph.D. Fellowship Program).



Hye-Soo Lee (S'17) received a B.S degree in materials science and engineering from the University of Seoul, Seoul, Korea in 2017. He is currently working toward a Ph.D. degree in materials science and engineering from Yonsei University, Seoul, Korea.

His current research interests include peptide aptamer-based biosensors, self-assembling biomolecules, organic-inorganic hybridized structure and bioactive nanostructures formation with chirality modified materials.



Yong-Beom Lim (M'01) received his B.S degree in Chemistry from SungKyunKwan University in 1995, and M.S and Ph.D. degrees in Chemistry from Seoul National University in 1997 and 2001, respectively. His postdoctoral research was done at the Department of Biochemistry & Biophysics, University of California, San Francisco (UCSF) (2002-2006). From 2006 to 2009, he worked at the Center for Supramolecular Nano-Assembly, Yonsei University as a research professor. He joined the MSE faculty of Yonsei University at 2009. He has pioneered the fields of biodegradable polymeric gene delivery carriers & bioactive self-assembling peptide nanostructures.

The focus of his current research is the development of self-assembling biomaterials based on the inspiration from nature, while combining principles of chemistry, biology, physics, medicine, and materials. He is on the Editorial Boards of Peptide Science and ChemPlusChem.



Youngcheol Chae (M'09-SM'19) received the B.S., M.S., and Ph.D. degrees in electrical and electronic engineering from Yonsei University, Seoul, South Korea in 2003, 2005 and 2009, respectively.

From 2009 to 2011, he was a post doctoral researcher with the Electronic Instrumentation Lab. of Delft University of Technology in the Netherlands. Since 2012, he has been on the faculty at Yonsei University and he is currently an Associate Professor. His work has focused on low-power data converters and high performance sensor interfaces.

This results in more than 80 technical papers and 30 patents.

He received the Best Young Professor Award in Engineering from Yonsei University in 2018. He received the Haedong Young Engineer Award from IEE Korea in 2017. He received the Outstanding Research Award of Yonsei University in 2017 and also received the Outstanding Teaching Awards of Yonsei University (2013 and 2014). He received a research grant from Samsung Research Funding Center in 2017 and a VENI grant from Dutch Technology Foundation STW in 2011. He is a member of the Technical Program Committees of International Solid-State Circuits Conference (ISSCC) and Asian Solid-State Circuits Conference (A-SSCC). He is a Distinguished Lecturer (DL) of IEEE Solid-State Circuits Society (SSCS).



Heonjin Choi (M'96) received the B.S., M.S., and Ph.D. degrees in ceramic engineering from Yonsei University, Seoul, Korea in 1986, 1988, and 1996.

From 1988 to 2004, he was a research scientist/senior research scientist in Korea institute of science and technology (KIST), Seoul, Korea. Also, he was a post-doctor in the department of Chemistry, University of California Berkeley, California, USA from 2002 to 2003. Since 2004, he has been a Faculty with Yonsei University, where he is currently a full professor. He has published more than

140 papers. His work has focused on biosensors using 1D, 2D, and 3D semiconducting nano/micro materials, fabrication of the nanodevice, neuro device, electroceuticals, photonics based on the 2D materials, and synthesis of nanomaterials.

Professor Choi is an editorial board of the nano journal and the open materials science journal. He is a member of the nano korea, the Korean ceramic society, and the Korea nano technology research society. He was a recipient of outstanding scientists from the outstanding scientists worldwide (JBC) in 2007. He was put on the list of Marquis' Who's Who in Asia/Science and Engineering in 2006, 2007.